



Elevated-Temperature 3D Printing of Hybrid Solid-State Electrolyte for Li-Ion Batteries

Meng Cheng, Yizhou Jiang, Wentao Yao, Yifei Yuan, Ramasubramonian Deivanayagam, Tara Foroozan, Zhennan Huang, Boao Song, Ramin Rojaee, Tolou Shokuhfar, Yayue Pan, Jun Lu, and Reza Shahbazian-Yassar*

While 3D printing of rechargeable batteries has received immense interest in advancing the next generation of 3D energy storage devices, challenges with the 3D printing of electrolytes still remain. Additional processing steps such as solvent evaporation were required for earlier studies of electrolyte fabrication, which hindered the simultaneous production of electrode and electrolyte in an all-3D-printed battery. Here, a novel method is demonstrated to fabricate hybrid solid-state electrolytes using an elevated-temperature direct ink writing technique without any additional processing steps. The hybrid solid-state electrolyte consists of solid poly(vinylidene fluoride-hexafluoropropylene) matrices and a Li⁺-conducting ionic-liquid electrolyte. The ink is modified by adding nanosized ceramic fillers to achieve the desired rheological properties. The ionic conductivity of the inks is $0.78 \times 10^{-3} \text{ S cm}^{-1}$. Interestingly, a continuous, thin, and dense layer is discovered to form between the porous electrolyte layer and the electrode, which effectively reduces the interfacial resistance of the solid-state battery. Compared to the traditional methods of solid-state battery assembly, the directly printed electrolyte helps to achieve higher capacities and a better rate performance. The direct fabrication of electrolyte from printable inks at an elevated temperature will shed new light on the design of all-3D-printed batteries for next-generation electronic devices.

Li-ion batteries have been widely used as the power source for electronic devices in the past two decades.^[1–3] The next-generation batteries are expected to be flexible, lightweight, low-cost, customizable, and be available in a variety of sizes.^[4–6] Although compelling efforts have been made in the development of both electrodes and electrolytes, the fabrication of a low-cost customized battery is regarded as one of the important challenges in the community.^[7–9] Conventionally, battery industry implements fabrication methods based on physical or chemical deposition since they are favorable for mass manufacturing. However, this has limited the complexity and diversity of batteries with respect to their size and shape.^[6] Among the existing technologies, additive manufacturing could be considered as the state-of-the-art technique to achieve the requirements of the next-generation batteries.^[9]

Additive manufacturing, also known as 3D printing, is an efficient method to manufacture products bottom-up with complex designs involving multilayer structures.^[10] Direct ink writing (DIW) is

one of the 3D printing techniques that has drawn worldwide attention due to its simple printing mechanisms and low-cost fabrication processes. Moreover, DIW has a wide range of materials selection, length scales, and an outstanding structural finish.^[11–13] The technique is expected to revolutionize technology in the fields of electronics,^[14,15] biotechnology,^[16–18] and medical science.^[19]


Recently, DIW was reported as one of the most promising methods for the fabrication of next-generation batteries with complex microstructures and high performances. Sun et al.^[20] and Fu et al.^[21] successfully fabricated Li-ion batteries with 3D interdigitated architectures. In Sun et al.'s work, a commercial liquid electrolyte was filled into the preprinted electrode, following which all the components were sealed.^[20] The performances of the microbattery were significantly improved by optimizing the design and fully utilizing the limited space. Fu et al. developed electrode inks by adding graphene oxide to modify the rheological properties.^[21] Hu et al. studied a special cathode ink of LiMn_{0.21}Fe_{0.79}PO₄ particles coated with carbon, which showed improved specific capacities

M. Cheng, Y. Jiang, Dr. Y. Yuan, R. Deivanayagam, T. Foroozan, Z. Huang, B. Song, R. Rojaee, Prof. Y. Pan, Prof. R. Shahbazian-Yassar
Department of Mechanical and Industrial Engineering
University of Illinois at Chicago
Chicago, IL 60607, USA
E-mail: rsyassar@uic.edu

W. Yao, Prof. R. Shahbazian-Yassar
Department of Mechanical Engineering-Engineering Mechanics
Michigan Technological University
Houghton, MI 49931, USA

Dr. Y. Yuan, Dr. J. Lu
Chemical Science and Engineering Division
Argonne National Laboratory
Chicago, IL 60439, USA

Prof. T. Shokuhfar
Department of Bioengineering
University of Illinois at Chicago
Chicago, IL 60607, USA

 The ORCID identification number(s) for the author(s) of this article can be found under <https://doi.org/10.1002/adma.201800615>.

DOI: 10.1002/adma.201800615

and high-rate performance.^[22] Kohlmeyer et al. prepared composite electrodes with different ratios of conductive additives and polymers with the utilization of a well-dispersed mixture of active materials and carbon nanofiber to make printable electrode inks.^[23] Besides electrode materials, 3D printing of solid-state electrolytes have also been reported over the past few years. Blake et al. demonstrated a porous polymer based separator with a good thermal stability and electrolyte wetting ability.^[24] McOwen et al. reported $\text{Li}_7\text{La}_3\text{Zr}_2\text{O}_{12}$ based inks with two binder systems that could be built into thin and intricate architectures after sintering.^[25] Zekoll et al. fabricated 3D structured templates using stereolithography and filled the templates with $\text{Li}_{1.4}\text{Al}_{0.4}\text{Ge}_{1.6}(\text{PO}_4)_3$ (LAGP). The LAGP scaffolds were prepared after removing the polymer template. A series of complex 3D structured hybrid electrolytes were obtained after filling the channels of the LAGP scaffolds with the polymer (polypropylene or epoxy).^[26] In all of the aforementioned contributions, post-treatment procedures such as heat treatment and freeze-drying were required to remove the solvent and template after printing. These postprocessing steps can cause distortion in the 3D structures even in cases where there is only a limited incorporation of solvents. Therefore, the large scale development of such printing inks for the battery industry can be extremely challenging.

In conventional battery manufacturing, the fabrication of electrolyte is an isolated process detached from that of the electrode. Printing the electrolyte directly onto the electrode via 3D printing technology could potentially reduce the fabrication time and the manufacturing cost. Electrolyte printing has been referred to as the bottleneck of printable battery manufacturing.^[27] The printed electrolyte is required to be adherent to the surrounding electrode layer in order to avoid shorting and to maintain the structural integrity during battery operation.^[27] In addition, in order to maintain the structural integrity of the 3D printed batteries, the printable electrolytes need to satisfy two requirements.^[11] First, the ink is required to have a proper viscosity to be extruded continuously from the nozzle and to be stacked layer-by-layer. Second, it is necessary to avoid shrinkage of the structure during solidification. Generally, solvent-evaporation and solidification are achieved by postprocessing heat treatments, which would change the shape of the electrolyte layer, leading to its shrinkage and eventual distortion.^[24,28] This shrinkage could potentially be minimized by printing the electrolyte directly onto the electrode.

Polymer-based electrolytes have high viscosities and low melting points, which make them ideal candidates for 3D printable inks. Safety issues such as flammability, and shorting due to dendrite growth are common in Li-ion batteries that use liquid electrolytes.^[29,30] The use of polymer electrolytes could effectively address such safety concerns in Li-ion batteries.^[31] Poly(vinylidene fluoride) (PVDF) based polymer electrolytes have good mechanical strength, thermal stability, and high anodic stability due to the presence of a strong electron-withdrawing functional group ($-\text{C}-\text{F}$).^[32,33] Moreover, poly(vinylidene fluoride-hexafluoropropylene) (PVDF-*co*-HFP) copolymer can achieve greater ionization of lithium salts with high dielectric constant, thereby providing a higher concentration of charge carriers.^[28] Recent studies of polymer electrolytes have reported that adding nanosized ceramics (TiO_2 , Al_2O_3 ,

SiO_2) can improve the physical and electrochemical properties of the electrolytes.^[30,34] Ionic liquids are one of the most promising molten salts to improve physicochemical properties such as safety, high-temperature stability, and ionic conductivity of the polymer-and-salt electrolyte system.^[35,36] In such polymer-and-salt systems, ionic liquids remain in liquid form which enhance the ionic conductivity and electrochemical properties.^[37] However, the poor interface between solid electrode and solid electrolyte leads to a high interfacial resistance.^[38–41] Building a dense layer between porous electrolyte and electrode has been reported as a way to reduce interfacial resistance. For instance, Fu et al. prepared such a garnet bilayer framework by laminating porous and dense taps.^[42]

In this report, we have engineered an elevated-temperature DIW 3D-printer from a robotic deposition system and designed a solid-state electrolyte ink to enable the 3D printing of hybrid solid-state electrolyte batteries. The hybrid electrolyte ink can be directly printed onto electrode without the need for any surface treatment of the substrate and postprocessing of the electrolyte. This would improve the efficiency of the preparation of the electrolyte and its incorporation into the battery. The hybrid solid-state electrolyte consists of the solid polymer matrix and ionic-liquid electrolyte. The solid polymer matrix enables Li-ion diffusion in addition to providing mechanical support that is sufficient enough to separate the electrodes. TiO_2 nanoparticles were added into the PVDF-*co*-HFP based polymer inks to modify their viscosity, tune the contact angles, and to improve the electrochemical performances. In addition, the 3D printed hybrid electrolyte created by the elevated-temperature DIW process shows lower interfacial resistance due to the formation of a unique dense interface between the electrolyte and electrode. Interestingly, the interfacial resistance in this method was reduced significantly compared with the traditional method of stacking the cast-electrolyte onto an electrode.

Figure 1a presents the solid electrolyte fabrication process by our elevated-temperature direct ink writing system. 3D architectures have been created by a robotic deposition system, which includes a three-axis direction stage, control system, pneumatic extrusion dispenser, fine cylindrical nozzle, and a self-designed heating block. The PVDF-*co*-HFP based polymer electrolyte ink was stored in syringes (Figure 1c) and kept at molten condition at 120 °C in the heat chamber (Figure 1b).

During the printing process, the three-axis direction stage moves at a moderate speed following a preprogrammed printing routine. The desired width and thickness of the printed electrolyte can be obtained by adjusting the air pressure, printing speed, and nozzle size. Extruded at a set pressure through a fine cylindrical nozzle, the molten electrolyte ink is directly deposited over a MnO_2 cathode substrate in an open-air environment under ambient conditions (Figure 1d and Movie S1, Supporting Information). The PVDF-*co*-HFP based ink solidifies once it reaches the substrate (Figure 1e). In this case, $\alpha\text{-MnO}_2$ electrode was used as the substrate for printing.

To fully utilize the ability of elevated-temperature direct writing, various structures were printed. While the spatial resolution and dimensionality have been reported as the limitations of fabrication methods such as screen-printing and ink-jet printing, our electrolyte could be fabricated even on a 3D surface.^[43] Figure 1f demonstrates a 3D-printed electrolyte

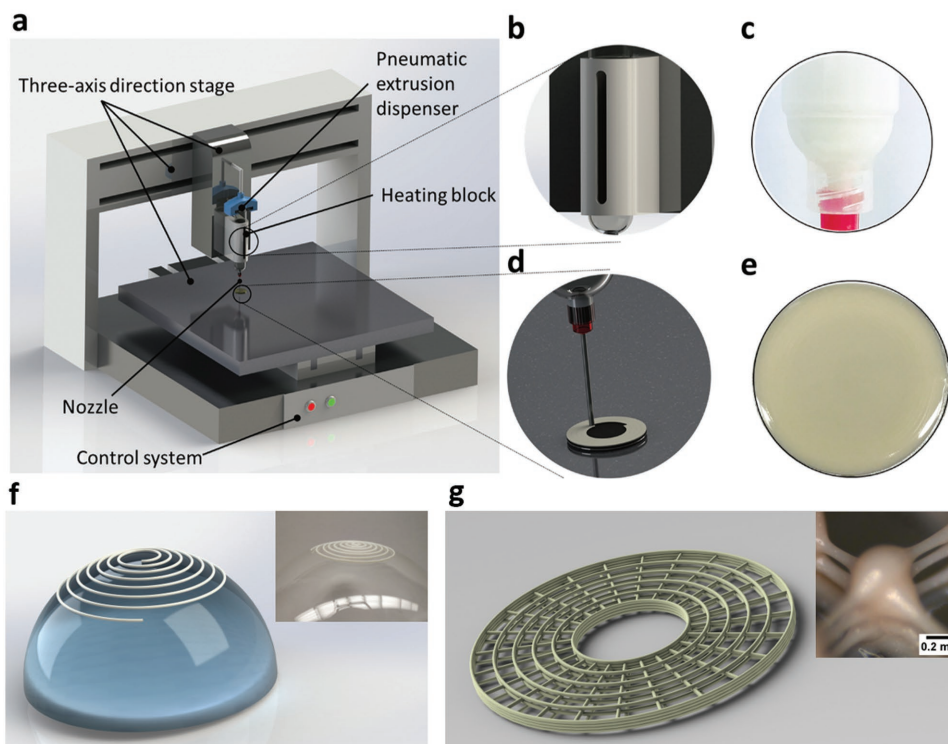


Figure 1. Schematic of the elevated-temperature direct ink writing system and solid-electrolyte ink fabrication process. a) Schematic showing the design of the developed robotic deposition system; b) schematic showing the zoom-in view of the heating chamber. c) Digital image of the molten solid-electrolyte inks stored in the syringe. d) Schematic showing that the solid-electrolyte is directly printed on electrode surface. e) Digital image of the printed electrolyte showing that the ink solidifies once it is printed on to the substrate at room temperature. f) Schematic of electrolyte that was printed onto a hemispherical surface, and digital image of the printed electrolyte (inset). g) Schematic of printed electrolyte with 3D radial array structure, and optical image of 3D electrolyte net (inset).

that was printed onto a hemispherical surface. As shown in Figure 1g, a 3D radial array was also successfully printed. The printed electrolyte formed a complex net structure with a self-supporting 3D scaffold. These structures do not require any postprocessing steps that are prone to induce shrinkage and structural damage. Thus, by printing the electrolyte ink onto uneven surfaces and sophisticated structures, we demonstrate that our proposed battery has the potential to be printed directly in electronic devices with complex shapes and limited space.

Our hybrid solid-state electrolyte ink consists of a polymer matrix containing a Li⁺-conducting ionic liquid.^[37] In this study, the Li⁺-conducting ionic liquid is composed of *N*-Propyl-*N*-methylpyrrolidinium bis(trifluoromethanesulfonyl)imide (Pyr₁₃TFSI) and lithium bis(trifluoromethanesulfonyl)imide (LiTFSI) salt. Hereafter, the Li⁺-conducting ionic-liquid electrolyte will be referred to as ILE. Poly(vinylidene fluoride-*co*-hexafluoropropylene) (PVDF-*co*-HFP) was dissolved into *N*-Methyl-2-pyrrolidone (NMP) solvent to form porous polymer matrices. Different proportions (2.5 and 5 wt%) of TiO₂ ceramic nanoparticles were used as fillers to increase the ionic conductivity and viscosity. The synthetic route of the hybrid solid-state electrolyte inks is shown in Figure 2. The ILE was added into PVDF-*co*-HFP/NMP mixture and stirred until the solution became transparent and homogeneous. The resulting composite electrolyte ink was heated at 90 °C for 50 hours to remove the NMP solvent, after which it assumed a solid-like

state. The removal of NMP was confirmed by obtaining the thermogravimetric analysis profile of the electrolyte INK-2 (Figure S1, Supporting Information). The ILE maintains liquid-like dynamics and fills the porous solid-state polymer matrix. Hereafter, the polymer electrolyte without ceramic fillers will be referred to as INK-0, and the nanocomposite electrolytes with 2.5 and 5 wt% TiO₂ will be denoted as INK-1 and INK-2, respectively.

The ability of an ink to be extruded from a nozzle and form a 3D pattern is highly dependent upon its rheological properties.^[12,13] Figure 3a plots the apparent viscosity of INK-0, INK-1, and INK-2 as a function of temperature. The measurements were performed at a constant strain of 1% and an angular frequency of 10 rad s⁻¹, while the inks were heated from 25 to 120 °C at the rate of 3 °C min⁻¹. Below 90 °C, the viscosity of all the inks decreased slowly with the increase in temperature. Note that there was an uncommon plateau followed by descending of INK-2 in the range of 70–90 °C, which might be caused by the TiO₂ aggregation.^[44] By adding a higher concentration of TiO₂, the nanoparticles could not be dispersed in the polymer as homogeneously as in the case of INK-1. The viscoelastic behavior of the aggregates led to INK-2 showing a solid-like behavior even at temperature range of 70–87 °C. At temperatures above 87 °C, the aggregates in INK-2 melted inducing a liquid-like viscoelastic behavior. When the temperature was further increased to certain regions (70–87 °C

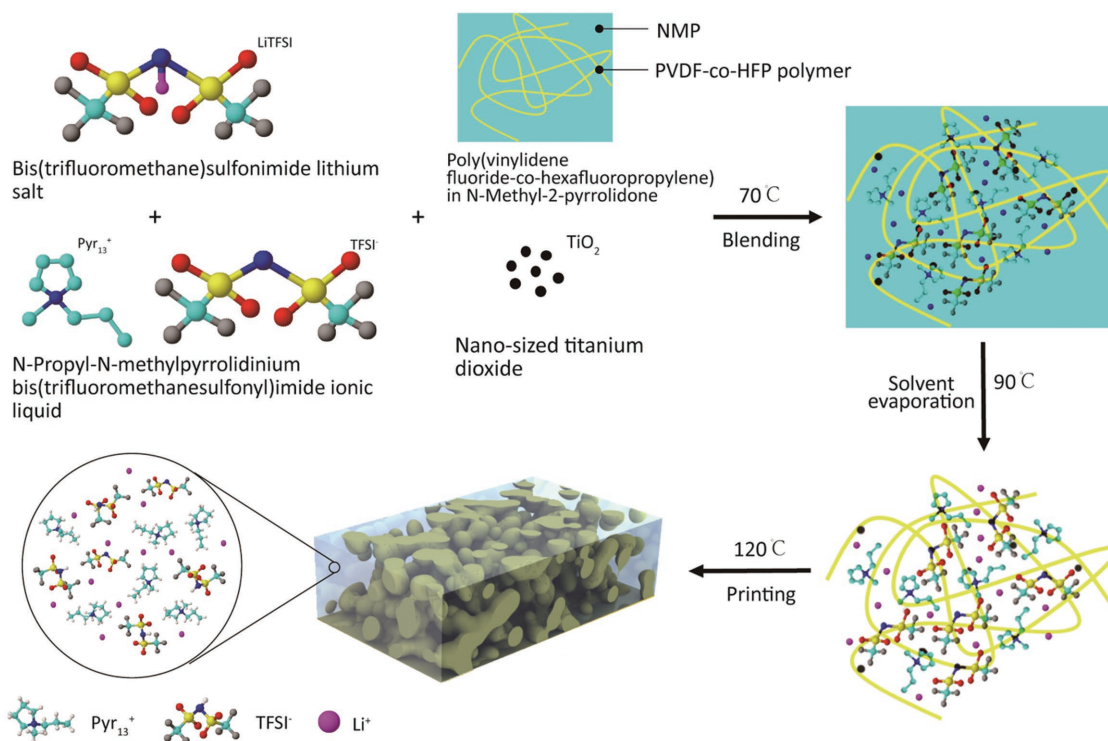


Figure 2. Schematic image showing the synthetic route of the PVDF-co-HFP/Pyr₁₃TFSI/LiTFSI/TiO₂ hybrid solid-state electrolyte ink.

for INK-0, and 100–115 °C for INK-1 and INK-2), the complex viscosity rose antithetically due to the coordination of Li⁺ ions with electron-withdrawing groups such as –CN that led to self-crosslinking.^[45] The curing temperatures of both the inks with nanoparticles, INK-1 and INK-2 increased to 113 and 114 °C. This indicated that the curing was delayed by the presence of TiO₂ nanoparticles.^[46] After the curing region, the viscosity of the ink experienced a rapid decrease, which indicated that the ink attained a viscous flow state. Hence, the printing temperature was set at 120 °C providing an ideal condition for the continuous formation of filaments without clogging during electrolyte printing. Figure 3b shows the apparent viscosity of the inks as a function of shear rate at 120 °C. All the inks exhibit shear-thinning behavior at 120 °C and a high apparent viscosity from 10⁴ to 10³ Pa s at a shear rate of 1 s⁻¹. The viscosity values of INK-1 and INK-2 were higher than that of INK-0, which suggests that the nanoparticles were responsible for the increase in viscosity. In addition, the viscosity of INK-1 was observed to be higher than that of INK-2. The reduction of viscosity when a higher concentration of nanoparticles is added, can be explained by the selective physisorption of high molar mass chains on the surface of TiO₂ nanoparticles and the decrease of the entanglement density.^[47] Figure 3c,d shows the storage modulus (*G'*) and loss modulus (*G''*) as a function of complex shear stress for INK-0, INK-1, and INK-2 at 120 °C. For the ink without fillers (INK-0), the loss modulus is larger than the storage modulus with the increase of shear stress from 0.1 to 10⁴ Pa (Figure 3c). This result indicates that the INK-0 maintains a liquid-like behavior in this region. The liquid-like behavior of INK-0 at high shear stress region is beneficial for the ink flow in the syringe and dispersion through

the nozzle during printing. On the other hand, the smaller storage modulus at low shear stress reflects that the printed ink cannot properly be stacked to form high-quality 3D structures along the nozzle movement. However, the inks with TiO₂ nanoparticles show a different behavior at 10⁻¹ to 10³ Pa in comparison to that of INK-0 (Figure 3d). In this region, the storage moduli (*G'*) of the inks are higher than the loss moduli (*G''*) indicating a solid-like behavior, which is beneficial for solidification during 3D printing. After the yield point, the viscous characteristics dominate, and the inks exhibit a liquid-like behavior in high shear stress region. In conclusion, the inks with TiO₂ nanoparticles can be extruded through the nozzle at high shear stresses, and exhibit a solid-like behavior after exiting the nozzle. Apart from viscosity, a large contact angle is another crucial property to guarantee successful printing of high-resolution 3D structures.^[48,49] However, the contact angle below 50° is conducive to a narrow line pattern.^[50] The contact angles for INK-0, INK-1, and INK-2 on MnO₂ electrode base (Figure 3e) are 38.4°, 47.8°, and 46.3°, respectively. The INK-1 and INK-2 have higher contact angles and are below 50°. Meanwhile, the contact angles below 90° reflect that the ink has an appreciable wettability, and therefore, spreads easily on a solid surface.^[51] The results indicate that a droplet formed by elevated-temperature DIW could wet the electrode surface completely. The good interfacial wetting between solid electrolyte and solid electrode can decrease the interfacial resistance and distribute the current at the interface evenly.^[52] It is noteworthy that the substrates were used directly without any additional surface treatments, making the overall battery fabrication process more efficient. Based on the evaluation of the rheology properties and contact angle results, it can be concluded

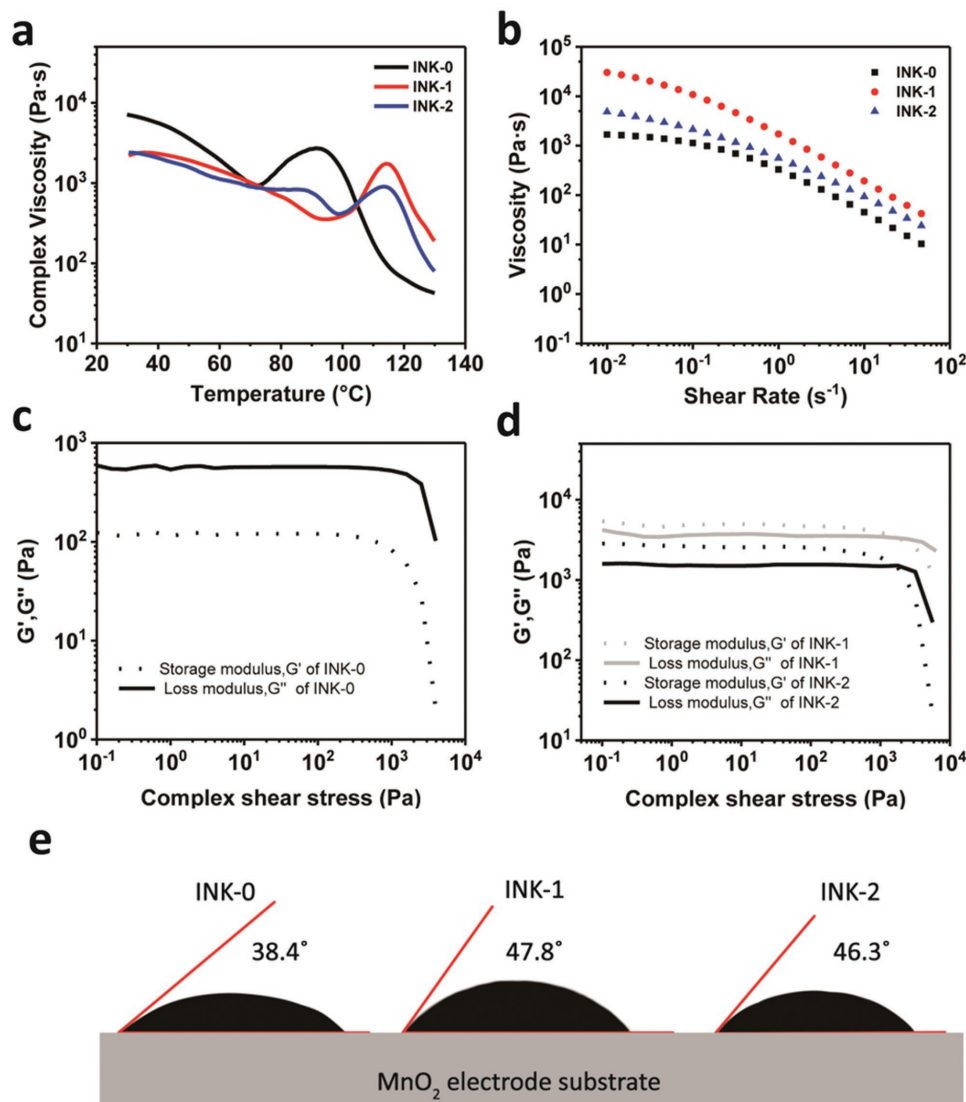


Figure 3. Properties of the polymer electrolyte inks. a) Complex viscosities of INK -0, INK -1, and INK -2 as a function of temperature. b) Apparent viscosities of INK -0, INK -1, and INK -2 as a function of shear rate at 120 °C. c,d) The storage modulus, G' , and loss modulus, G'' , as a function of complex shear stress for INK-0 (c) and INK-1 and INK-2 (d). e) Contact angles for INK-0, INK-1, and INK-2 on MnO_2 electrode substrate.

that the INK-1 and INK-2 are more suitable for the elevated-temperature DIW process.

The surface morphology of the printed electrolyte was characterized by scanning electron microscopy (SEM). The dimension of pores in the polymer electrolytes is about 10–20 nm, and the ion sizes of Pyr_{13}^+ and TFSI^- are calculated based on the ball and stick model of ions (Figure S2, Supporting Information). The longest dimensions for Pyr_{13}^+ and TFSI^- are 0.72 and 0.79 nm, respectively.^[37] Since the distributed micro-sized pores are much larger than the dimension of Pyr_{13}^+ and TFSI^- , the pores have the capability to accommodate the ILE (Figure 4a). The flat morphology of the surface of the INK-2 indicates that the ILE remains immobilized in the structure of micropores (Figure 4b). A schematic diagram of the printed hybrid solid-state electrolyte is shown in Figure 4c. Even after the polymer-based electrolyte inks were printed on the electrode, the ILE maintains its liquid dynamics while solid-state

polymer matrix provides the network for Li^+ conduction and mechanical support.

Figure 4d shows the cross-sectional SEM image of the electrolyte after washing out the ILE. A dense layer was found between the cluster-like porous PVDF-co-HFP electrolyte layer and the $\alpha\text{-MnO}_2$ electrode layer. The EDS mapping (Figure S3, Supporting Information) suggests that the formation of the dense layer could be attributed to the PVDF-co-HFP that was melted during the elevated-temperature DIW process. The dense layer provides a close contact between the electrolyte and the electrode (Figure 4e). This phenomenon could be observed in the cases of INK-0 and INK-1 as well (Figure S4b–d, Supporting Information). The reason for the dense layer formation could be explained by the fact that PVDF-co-HFP is a fluorinated copolymer of PVDF, which is also the binder material used in MnO_2 electrode. The molten PVDF-co-HFP in the electrolyte has a noticeable affinity toward the binder in the

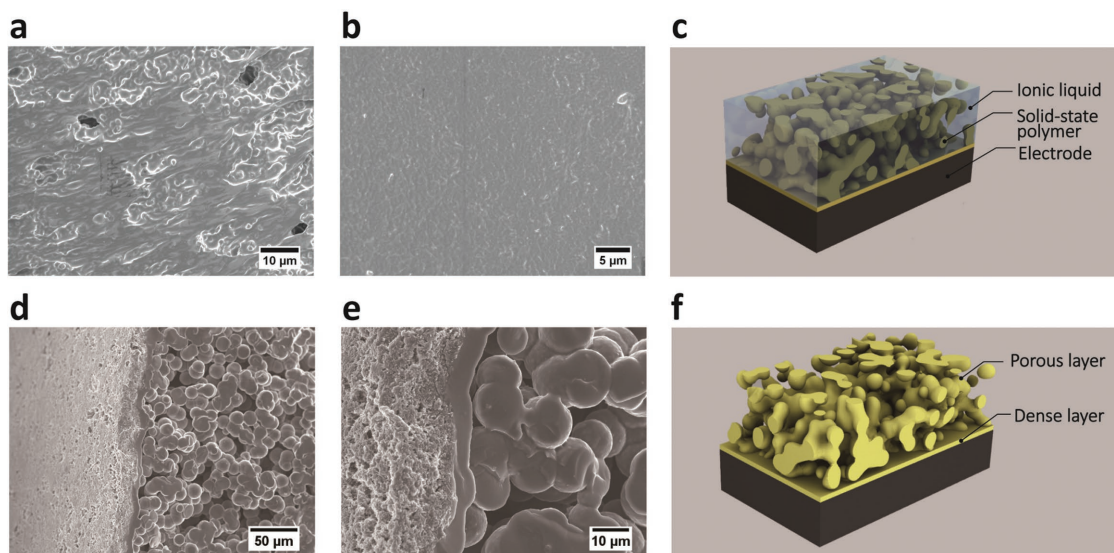


Figure 4. Structure of the printed electrolyte (INK-2). SEM images of a) cross-section and b) surface of the printed electrolyte. c) Schematic of the printed hybrid solid-state electrolyte. d) Cross-sectional SEM image of the printed electrolyte after washing out the ILE. e) SEM image of the dense layer between the porous layer and the MnO₂ electrode. f) Schematic of the bilayer structure of the printed solid-state electrolyte.

electrode.^[53,54] This was evident when the polymer was printed onto a stainless-steel substrate without the binder. No dense layer could be observed in this case (Figure S4a, Supporting Information). Therefore, we believe that there are two prerequisites to be met for the formation of the dense layer. First, the electrolyte ink needs to be a copolymer of the binder material in the substrate. Second, the electrolyte has to be in molten state for the formation of the dense layer. Figure 4f shows a schematic of the bilayer structure of the printed solid-state electrolyte with α -MnO₂ electrode.

Ionic conductivity is a crucial property that determines the electrochemical performance of solid-state electrolytes. A symmetric cell configuration comprising the hybrid solid-state electrolyte sandwiched between two stainless-steel blocking electrodes was used to measure the ionic conductivities. The ionic conductivity measurements of the electrolytes with different electrolyte compositions are shown in Figure 5a. The ionic conductivity was calculated using the relation, $\sigma = D \times R_b^{-1} \times A^{-1}$, where D is the thickness of electrolyte, R_b is the bulk resistance from the impedance plot, and A is the surface area of the electrolyte layer that is in contact with the electrode. The ionic conductivity of the inks, INK-0, INK-1, and INK-2 were 5.81×10^{-5} , 0.49×10^{-3} , and 0.78×10^{-3} S cm⁻¹, respectively. The increase of the ionic conductivity upon addition of the nanoparticle fillers, could be explained by the Lewis acid-base interactions between the polymer and the inorganic nanoparticle fillers. The interactions between Lewis acidic sites on the surface of inorganic fillers and the polymer contribute to the release of more free Li⁺ ions.^[55–57] The Fourier transform infrared (FT-IR) spectra of the inks indicate that the inks with a higher concentration of nanoparticles have a higher ratio of free Li⁺ ions to the paired ions in the electrolyte (Figure S5, Supporting Information). Earlier studies also report a critical concentration value of ceramics fillers at around 5 wt%.^[58]

Next, we assembled the solid-state Li-ion battery by two different approaches. One was the conventional method where

a preprepared electrolyte was stacked with cathode and anode electrodes. The other method was to directly stack a printed-electrolyte/electrode onto a Li foil as reference/counter electrode to form a half-cell. α -MnO₂ material was selected as the cathode for both cases. In case of the electrolyte obtained by casting technique, the thickness (height) cannot be tuned to desirable values. However, using the printing technique, the thickness of the electrolyte could be accurately controlled by adjusting any of the dispensing parameters such as the air pressure, printing speed, or the nozzle size. The experimental details are provided in Table S2 and Figure S6 (Supporting Information). Figure 5b–d represents the electrochemical impedance spectroscopy (EIS) tests conducted on printed and cast hybrid Li-ion batteries. The EIS tests were performed after 10 cycles of cyclic voltammetry (Figure S7, Supporting Information). An equivalent circuit was applied to fit the data of impedance spectra. In the equivalent circuit, R_s indicates the bulk resistance of the cell, which includes the electrode, electrolyte, and the membrane. R_{int} represents the resistance of the interface between electrode and electrolyte, and R_{ct} represents the charge transfer resistance.^[59] Normally, the porous structure of polymer electrolytes reduces the contact area with the electrodes, which results in high interfacial resistance and impedes the Li-ion transport.^[42] Interestingly, comparing the batteries fabricated by the two approaches, the interfacial resistance of the printed hybrid electrolytes were smaller than those of casted electrolytes in the mid-frequency region (Table S3, Supporting Information). Our results show that the dense layer formed by elevated-temperature DIW provides a close contact between the solid-state electrolyte and electrode, which reduces the interfacial resistance.

Figure 6 shows the electrochemical performances of cells with hybrid structure solid-state electrolyte. The α -MnO₂/Li half-cells were tested in a voltage range of 1.5–4.0 V. The capacity values have been normalized to the mass of α -MnO₂. Figure 6a shows the charge and discharge curves of α -MnO₂/Li half-cells

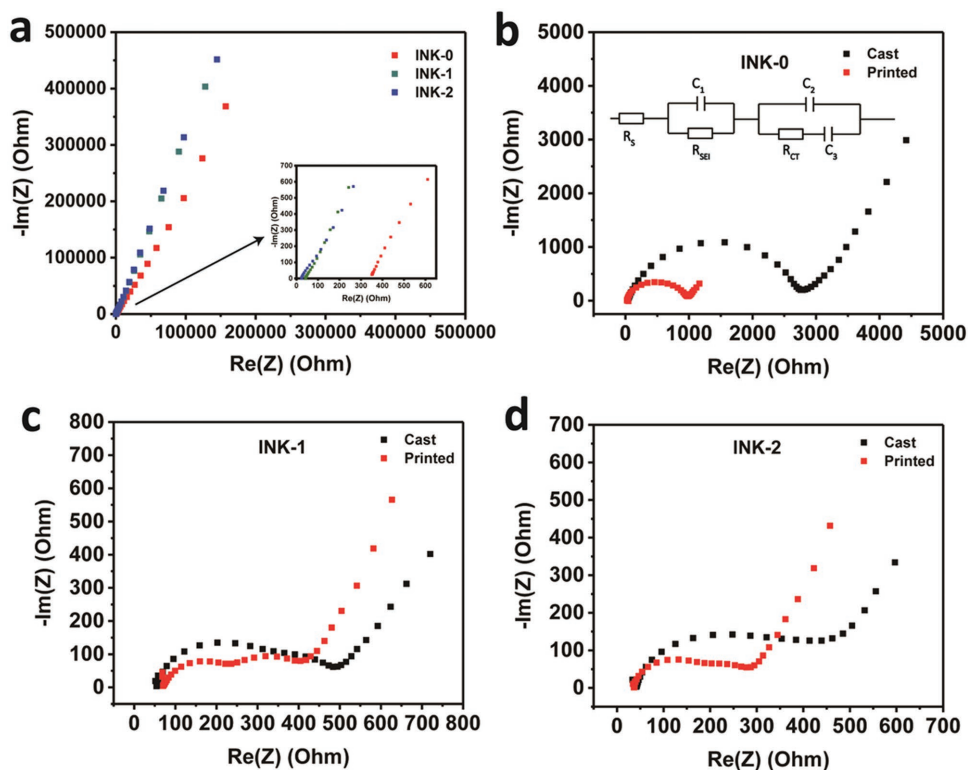


Figure 5. Electrochemical impedance spectroscopy (EIS) test of hybrid solid-state electrolyte: a) impedance spectra of the printed inks sandwiched between two steel blocking electrodes. Impedance spectra for inks with α - MnO_2/Li half cells with: b) printed INK-0, cast INK-0, and the equivalent circuit (inset), c) printed INK-1 and cast INK-1, and d) printed INK-2 and cast INK-2.

assembled with the printed hybrid electrolytes at a specific current of 16 mA g^{-1} . All the samples exhibit a discharge reaction around 2.7 V and a charge reaction around 3.2 V , which are related to lithium intercalation and deintercalation of the tunnel-structured metal oxides respectively.^[60] The discharge capacity of battery cells assembled with the printed INK-2 electrolyte was 127.3 mAh g^{-1} , which was $\approx 12\%$ and 11% higher than the capacity of the cell with printed INK-0 (113.7 mAh g^{-1}) and INK-1 (115.1 mAh g^{-1}), respectively. The cells with the cast INK-2 electrolyte also presented a higher charge capacity than that of the INK-0 and INK-1 (Figure S8, Supporting Information). The coulombic efficiency of the first cycle is low in all the three cases due to high initial irreversible capacity. All the cells have a stable reversible capacity after the first cycle (Figure S9, Supporting Information).

Figure 6b shows the rate profile of the printed INK-2 and cast INK-2 within the range of 32 to 480 mA g^{-1} . Figure 6c–d shows the first-cycle voltage profiles of the printed and cast INK-2 at different specific currents. The capacity values of the printed electrolyte are higher than that of the cast electrolyte at each rate, which is ascribed to the good contact between the electrolyte and the electrode, leading to a lower interfacial resistance. Moreover, the printed electrolyte recovered to 98.4% of initial specific capacity after returning to the low specific current, and this value is much higher than that of the cast electrolyte (92.7%). The average coulombic efficiency (Figure 6e) of the cell assembled with a printed INK-2 hybrid electrolyte is maintained at 98.6% over 100 cycles, indicating that the cell

has a good cycling stability. Figure 6f shows the SEM image of the electrolyte recovered after cycling. No obvious change of the dense layer could be observed even after 100 cycles suggesting that the dense layer is stable during charge/discharge cycles. The good stability of the transitioning layer upon cycling is critical for maintaining the battery performance over its life cycle.

Figure 6g,h shows the digital and optical images of the 3D-printed interdigitated full cell battery. Lithium iron phosphate (LiFePO_4 , LFP) and lithium titanium oxide ($\text{Li}_4\text{Ti}_5\text{O}_{12}$, LTO) electrodes were printed in six layers with a total thickness of 1.2 mm . The size of the interdigitated architecture is $10 \text{ mm} \times 5 \text{ mm}$. The mass loading of the cathode and anode are 2.1 and 2.3 mg , respectively. INK-2 was printed into the channels between the electrodes. After the electrodes were dried, carbon paste was applied as the current collector. Lastly, polydimethylsiloxane (PDMS) gel was used to seal the cell inside an argon-filled glove box. The performance of the full cell battery was tested at the specific current of 16 mA g^{-1} (Figure S10, Supporting Information). The initial charge and discharge capacities were 148 and 112 mAh g^{-1} , respectively, leading to the coulombic efficiency of 75.6% . The second charge and discharge capacities were 95 and 95 mAh g^{-1} , respectively, indicating an increase in the coulombic efficiency to 100% . Moreover, a full cell with a 3D Hilbert curved structure was printed (Figure 6i). LFP and LTO materials that were printed onto preprinted PDMS substrates, were used as the cathode and anode, respectively. The INK-2 was used as the electrolyte and was printed between the cathode and anode. After the

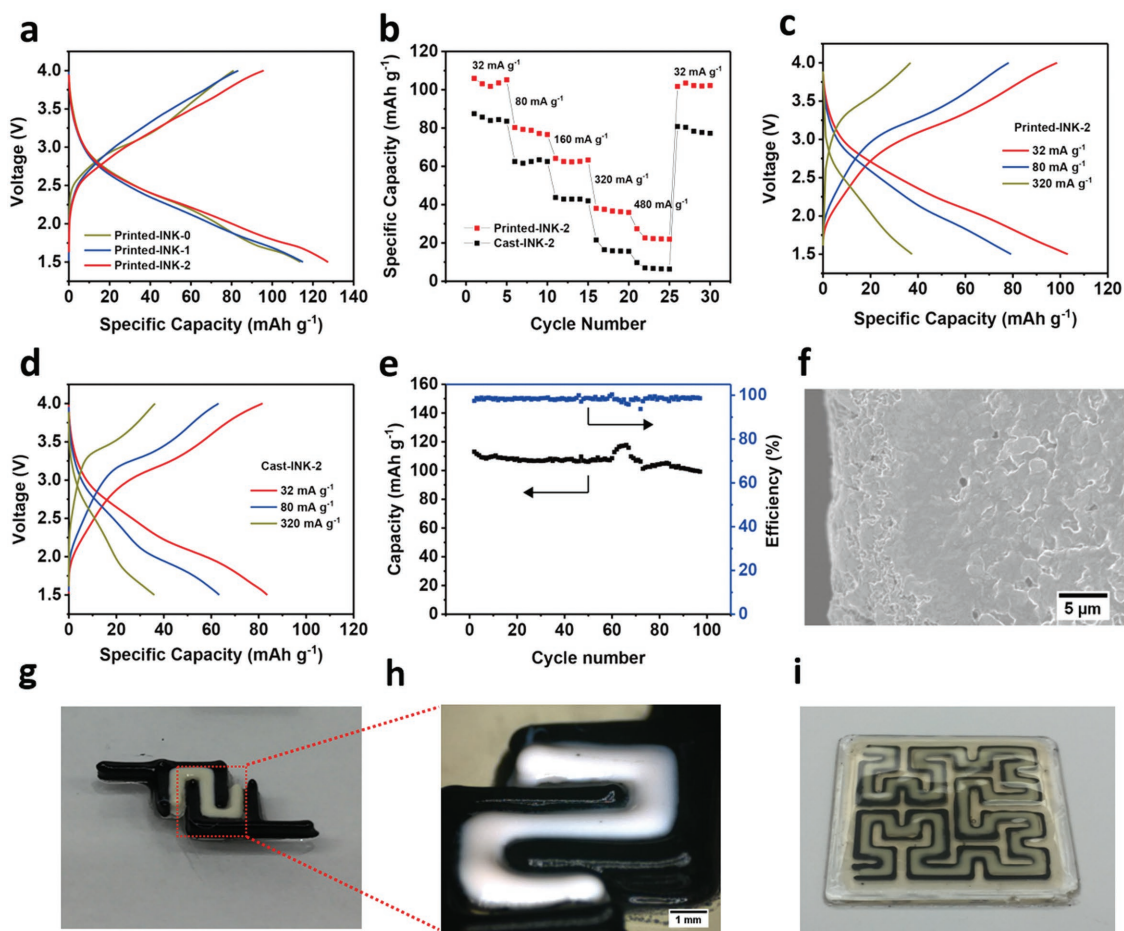


Figure 6. Electrochemical characterization of the printed electrolyte: a) First-cycle charge–discharge voltage profiles of MnO_2/Li with printed electrolyte at a specific current of 16 mA g^{-1} . b) Rate profile of Li/MnO_2 half-cell with printed/cast INK-2 electrolyte at various specific currents. c) Voltage profile of Li/MnO_2 half-cell with printed INK-2 at various specific currents. d) Voltage profile of Li/MnO_2 half-cell with cast INK-2 at various specific currents. e) Cycling performance of the $\text{Li}/\text{INK-2}/\text{MnO}_2$ half-cell at 16 mA g^{-1} . f) Cross-sectional SEM image of the printed electrolyte after 100 cycles. g) Digital and (h) optical image of the 3D-printed interdigitated full cell battery composed of $\text{LTO}/\text{INK-2}/\text{LFP}$. i) Optical image of the 3D-printed Hilbert curved structure full cell battery composed of $\text{LTO}/\text{INK-2}/\text{LFP}$.

electrodes were dried, the structure was sealed with PDMS gel. This proof-of-concept demonstrates that the battery has the potential to be printed in any shape, opening new opportunities to implement this technology for power sources in electronic devices with complex circuits.

In conclusion, we report direct 3D printing of polymer-based inks on battery electrodes with an elevated-temperature extrusion robot. The PVDF-co-HFP based inks with nanosized TiO_2 fillers exhibited shear-thinning behavior, high apparent viscosities, desirable contact angles, and very good wettability with the electrode substrates. The electrolytes produced by elevated-temperature 3D printing can be directly printed onto the electrode surfaces without the need for any surface preparation. In addition, this high-temperature printing method prevents the typical shrinkage and loss of structural integrity that are the drawbacks of other fabrication techniques. During the elevated-temperature printing, a dense layer was formed between the porous polymer-based electrolyte and the electrode. This dense layer was found to significantly reduce the interfacial resistance. The batteries with the printed electrolytes showed

higher charge/discharge capacity values and a better rate performance than the batteries where electrolyte was fabricated by the traditional solution-casting method. The average coulombic efficiency was maintained at 98.6% for over 100 cycles using the DIW printed solid electrolyte. The elevated-temperature direct writing and synthesis of the inks in this work would provide inspiration for the development of conformal and readily fabricated solid-state power sources.

Supporting Information

Supporting Information is available from the Wiley Online Library or from the author.

Acknowledgements

R.S.-Y. acknowledges the financial support from the National Science Foundation (No. DMR-1620901). Partial funding for Y.Y. from Argonne National Laboratory under subcontract No. 4J-30361 is acknowledged.

W.Y. acknowledges Multi-Scale Technologies Institute at Michigan Technological University. M.C. acknowledges China Scholarship Council (CSC). R. S.-Y. and Y.P. are thankful to the Battery Cluster support from the UIC College of Engineering and MIE Department.

Conflict of Interest

The authors declare no conflict of interest.

Keywords

3D printing, hybrid, interfacial study, Li-ion battery, solid-state electrolyte

Received: January 29, 2018

Revised: June 15, 2018

Published online: August 21, 2018

-
- [1] M. Armand, J.-M. Tarascon, *Nature* **2008**, 451, 652.
- [2] A. S. Arico, P. Bruce, B. Scrosati, J.-M. Tarascon, W. Van Schalkwijk, *Nat. Mater.* **2005**, 4, 366.
- [3] G. Bruce, B. Scrosati, J.-M. Tarascon, *Angew. Chem., Int. Ed.* **2008**, 47, 2930.
- [4] G. Zhou, F. Li, H.-M. Cheng, *Energy Environ. Sci.* **2014**, 7, 1307.
- [5] J. F. M. Oudenhoven, R. J. M. Vullers, R. Schaijk, *Int. J. Energy Res.* **2012**, 36, 1139.
- [6] F. Zhang, M. Wei, V. V. Viswanathan, B. Swart, Y. Shao, G. Wu, C. Zhou, *Nano Energy* **2017**, 40, 418.
- [7] H. Li, Z. Wang, L. Chen, X. Huang, *Adv. Mater.* **2009**, 21, 4593.
- [8] B. Scrosati, J. Garche, *J. Power Sources* **2010**, 195, 2419.
- [9] X. Tian, J. Jin, S. Yuan, C. K. Chua, S. B. Tor, K. Zhou, *Adv. Energy Mater.* **2017**, 7, 1700127.
- [10] S. H. Huang, P. Liu, A. Mokasdar, L. Hou, *Int. J. Adv. Manuf. Technol.* **2012**, 67, 1191.
- [11] J. A. Lewis, *Adv. Funct. Mater.* **2006**, 16, 2193.
- [12] K. K. B. Hon, L. Li, I. M. Hutchings, *CIRP Ann. – Manuf. Technol.* **2008**, 57, 601.
- [13] J. A. Lewis, G. M. Gratson, *Mater. Today* **2004**, 7, 32.
- [14] D. Espalin, D. W. Muse, E. MacDonald, R. B. Wicker, *Int. J. Adv. Manuf. Technol.* **2014**, 72, 963.
- [15] E. Macdonald, R. Salas, D. Espalin, M. Perez, E. Aguilera, D. Muse, R. B. Wicker, *IEEE Access* **2014**, 2, 234.
- [16] B. C. Gross, J. L. Erkal, S. Y. Lockwood, C. Chen, D. M. Spence, *Anal. Chem.* **2014**, 86, 3240.
- [17] V. Mironov, T. Boland, T. Trusk, G. Forgacs, R. R. Markwald, *Trends Biotechnol.* **2003**, 21, 157.
- [18] F. P. Melchels, M. A. Domingos, T. J. Klein, J. Malda, P. J. Bartolo, D. W. Huttmacher, *Prog. Polym. Sci.* **2012**, 37, 1079.
- [19] F. Rengier, A. Mehndiratta, H. von Tengg-Kobligk, C. M. Zechmann, R. Unterhinninghofen, H.-U. Kauczor, F. L. Giesel, *Int. J. Comput. Assist. Radiol. Surg.* **2010**, 5, 335.
- [20] K. Sun, T. S. Wei, B. Y. Ahn, J. Y. Seo, S. J. Dillon, J. A. Lewis, *Adv. Mater.* **2013**, 25, 4539.
- [21] K. Fu, Y. B. Wang, C. Y. Yan, Y. G. Yao, Y. A. Chen, J. Q. Dai, S. Lacey, J. Y. Wan, T. Li, Z. Y. Wang, Y. Xu, L. B. Hu, *Adv. Mater.* **2016**, 28, 2587.
- [22] J. Hu, Y. Jiang, S. Cui, Y. Duan, T. Liu, H. Guo, L. Lin, Y. Lin, J. Zheng, K. Amine, F. Pan, *Adv. Energy Mater.* **2016**, 6, 1600856.
- [23] R. R. Kohlmeier, A. J. Blake, J. O. Hardin, E. A. Carmona, J. Carpena-Núñez, B. Maruyama, J. Daniel Berrigan, H. Huang, M. F. Durstock, *J. Mater. Chem. A* **2016**, 4, 16856.
- [24] A. J. Blake, R. R. Kohlmeier, J. O. Hardin, E. A. Carmona, B. Maruyama, J. D. Berrigan, H. Huang, M. F. Durstock, *Adv. Energy Mater.* **2017**, 7, 1602920.
- [25] D. W. McOwen, S. Xu, Y. Gong, Y. Wen, G. L. Godbey, J. E. Gritton, T. R. Hamann, J. Dai, G. T. Hitz, L. Hu, E. D. Wachsman, *Adv. Mater.* **2018**, 30, e1707132.
- [26] S. Zekoll, C. Marriner-Edwards, A. K. O. Hekselman, J. Kasemchainan, C. Kuss, D. E. J. Armstrong, D. Cai, R. J. Wallace, F. H. Richter, J. H. J. Thijssen, P. G. Bruce, *Energy Environ. Sci.* **2018**, 11, 185.
- [27] A. Vlad, N. Singh, C. Galande, P. M. Ajayan, *Adv. Energy Mater.* **2015**, 5, 1402115.
- [28] J. Song, Y. Wang, C. C. Wan, *J. Power Sources* **1999**, 77, 183.
- [29] J. K. Kim, J. Scheers, T. J. Park, Y. Kim, *ChemSusChem* **2015**, 8, 636.
- [30] A. Manuel Stephan, K. S. Nahm, *Polymer* **2006**, 47, 5952.
- [31] X. X. Zeng, Y. X. Yin, N. W. Li, W. C. Du, Y. G. Guo, L. J. Wan, *J. Am. Chem. Soc.* **2016**, 138, 15825.
- [32] F. Liu, N. A. Hashim, Y. Liu, M. R. M. Abed, K. Li, *J. Membr. Sci.* **2011**, 375, 1.
- [33] L. Xie, X. Huang, K. Yang, S. Li, P. Jiang, *J. Mater. Chem. A* **2014**, 2, 5244.
- [34] Z. H. Li, H. P. Zhang, P. Zhang, G. C. Li, Y. P. Wu, X. D. Zhou, *J. Membr. Sci.* **2008**, 322, 416.
- [35] I. Osada, H. de Vries, B. Scrosati, S. Passerini, *Angew. Chem., Int. Ed. Engl.* **2016**, 55, 500.
- [36] Y.-S. Ye, J. Rick, B.-J. Hwang, *J. Mater. Chem. A* **2013**, 1, 2719.
- [37] G. Tan, F. Wu, C. Zhan, J. Wang, D. Mu, J. Lu, K. Amine, *Nano Lett.* **2016**, 16, 1960.
- [38] J.-K. Kim, Y. J. Lim, H. Kim, G.-B. Cho, Y. Kim, *Energy Environ. Sci.* **2015**, 8, 3589.
- [39] J. Liu, Z. Xu, X. Li, Y. Zhang, Y. Zhou, Z. Wang, X. Wang, *Sep. Purif. Technol.* **2007**, 58, 53.
- [40] S. Xin, Y. You, S. Wang, H.-C. Gao, Y.-X. Yin, Y.-G. Guo, *ACS Energy Lett.* **2017**, 2, 1385.
- [41] H. Duan, Y. X. Yin, Y. Shi, P. F. Wang, X. D. Zhang, C. P. Yang, J. L. Shi, R. Wen, Y. G. Guo, L. J. Wan, *J. Am. Chem. Soc.* **2018**, 140, 82.
- [42] K. Fu, Y. Gong, G. T. Hitz, D. W. McOwen, Y. Li, S. Xu, Y. Wen, L. Zhang, C. Wang, G. Pastel, J. Dai, B. Liu, H. Xie, Y. Yao, E. D. Wachsman, L. Hu, *Energy Environ. Sci.* **2017**, 10, 1568.
- [43] J. J. Adams, E. B. Duoss, T. F. Malkowski, M. J. Motala, B. Y. Ahn, R. G. Nuzzo, J. T. Bernhard, J. A. Lewis, *Adv. Mater.* **2011**, 23, 1335.
- [44] P. Cassagnau, *Polymer* **2013**, 54, 4762.
- [45] W. Li, M. Yuan, M. Yang, *Eur. Polym. J.* **2006**, 42, 1396.
- [46] S. Park, N. Bernet, S. De La Roche, H. Hahn, *J. Compos. Mater.* **2003**, 37, 465.
- [47] S. Jain, J. G. P. Goossens, G. W. M. Peters, M. van Duin, P. J. Lemstra, *Soft Matter* **2008**, 4, 1848.
- [48] B. K. Park, D. Kim, S. Jeong, J. Moon, J. S. Kim, *Thin Solid Films* **2007**, 515, 7706.
- [49] W. Yu, H. Zhou, B. Q. Li, S. Ding, *ACS Appl. Mater. Interfaces* **2017**, 9, 4597.
- [50] S. Jeong, H. C. Song, W. W. Lee, S. S. Lee, Y. Choi, W. Son, E. D. Kim, C. H. Paik, S. H. Oh, B. H. Ryu, *Langmuir* **2011**, 27, 3144.
- [51] T. Tanaka, J. Lee, P. R. Scheller, in *Treatise on Process Metallurgy* (Ed: S. Seetharaman), Elsevier, Boston, MA, USA **2014**, p. 61.
- [52] K. K. Fu, Y. Gong, B. Liu, Y. Zhu, S. Xu, Y. Yao, W. Luo, C. Wang, S. D. Lacey, J. Dai, *Sci. Adv.* **2017**, 3, e1601659.
- [53] G. T. Pickett, A. C. Balazs, *Macromol. Theory Simul.* **1998**, 7, 249.
- [54] C. Kellogg, D. Walton, A. Mayes, P. Lambooy, T. Russell, P. Gallagher, S. Satija, *Phys. Rev. Lett.* **1996**, 76, 2503.
- [55] F. Croce, G. Appetecchi, L. Persi, B. Scrosati, *Nature* **1998**, 394, 456.

- [56] S. Mogurampelly, O. Borodin, V. Ganesan, *Annu. Rev. Chem. Biomol. Eng.* **2016**, *7*, 349.
- [57] J.-K. Kim, G. Cheruvally, X. Li, J.-H. Ahn, K.-W. Kim, H.-J. Ahn, *J. Power Sources* **2008**, *178*, 815.
- [58] J. Cao, L. Wang, Y. Shang, M. Fang, L. Deng, J. Gao, J. Li, H. Chen, X. He, *Electrochim. Acta* **2013**, *111*, 674.
- [59] S. S. Zhang, K. Xu, T. R. Jow, *Electrochim. Acta* **2006**, *51*, 1636.
- [60] Y. Yuan, C. Zhan, K. He, H. Chen, W. Yao, S. Sharifi-Asl, B. Song, Z. Yang, A. Nie, X. Luo, H. Wang, S. M. Wood, K. Amine, M. S. Islam, J. Lu, R. Shahbazian-Yassar, *Nat. Commun.* **2016**, *7*, 13374.